Local Environment Affects Activity of Enzymes on 3D Molecular Scaffold

Yan Xiong¹, James Huang², Shih-Ting Wang³, Sufi Zafar^{4*}, Oleg Gang^{1,2,3**}

¹Department of Chemical Engineering, Columbia University, New York, NY 10027, USA

²Department of Applied Physics and Applied Mathematics, Columbia University, New York, NY 10027, USA

³Center for Functional Nanomaterials, Brookhaven National Laboratory, Upton, NY 11973, USA

⁴IBM T.J. Watson Research Center, Yorktown Heights, New York 10589, USA

*Sufi Zafar (phone: (914) 803-2981; Email: szafar@us.ibm.com)

**Oleg Gang (phone: (631) 278-3778; Email: og2226@columbia.edu)

ABSTRACT

Ability of coordinating and confining enzymes presents opportunity to affect their performance and to create chemically active materials. Recent studies show that polymers and biopolymers can be used to scaffold enzymes and that can lead to the modulated biocatalytic efficiency. Here, we investigated the role of micro-environments on enzyme activity using a well-defined molecular scaffold. An enzyme, glucose oxidase (GOx), was positioned at different locations of a three-dimensional (3D) octahedral DNA scaffold (OS), allowing to alter enzyme's polyanionic environments. Using electrical sensing, based on a bipolar junction transistor, we measured directly and in real-time enzyme's proton generation at these different micro-environments. We found a 200% enhancement of immobilized enzyme over free GOx, and about 30 % increase in catalytic rates when enzyme is moved on the same molecular scaffold to a micro-environment with a higher local concentration of polyanions, which suggests a role of local pH on the enzymatic activity.

KEYWORDS

enzymes, DNA nanotechnology, molecular scaffolds, self-assembly, micro-environments.

Enzyme confinement and compartmentalization are general strategies found in the nature to control substrate specificity, prevent unwanted off-target reactions, and concentrate biochemical reactions.¹ Inspired by nature, the catalytic properties of surface and volume-confined enzymes have further been studied for the understanding of complex cellular pathways, and for enhancing enzymatic activities through engineering of their structures.^{2, 3} Several approaches to modulate enzymatic activities by physical adsorption and covalent crosslinking of enzymes onto bioactive surfaces have also been developed.⁴⁻⁶ For example, metal—organic frameworks offer a porous surface for physically immobilizing enzymes through surface attachment and pore encapsulation, as well as covalently anchoring enzymes mediated by carboxylate activating molecules.⁷ Besides, an ability to manipulate biocatalytic cascades using a magnetic field that can affect local environments was recently shown.⁸

Designed molecular scaffolds offer tremendous opportunity for manipulating enzymatic cascades⁹, but require ability to create desired scaffold architectures, place of enzymes specifically and control of local physiochemical properties of scaffolds. In this respect, DNA nanotechnology, which utilizes molecular plasticity and intermolecular connectivity to program DNA architectures, ¹⁰⁻¹⁴ has been exploited as a promising scaffold material ¹⁵⁻¹⁹ for tailoring enzymatic reactions and activities. ²⁰⁻²⁵ Researchers have reported that a DNA origami scaffold can significantly enhance the catalytic activities of serial enzymatic reactions, such as glucose oxidase (GOx)- horseradish peroxidase (HRP) cascade with 15 folds of activity enhancement²⁶ in a small confined space. ^{12, 13, 27} Recently, it was shown that GOx-HPR enzymes cascades can be rationally organized into 3D nanostructured arrays using a DNA-based material voxel strategy: such organization leads to an enhanced activity of the cascades. ²⁸

Two possible mechanisms have been proposed to discuss the observed enhancement of enzymatic activities on DNA-based scaffolds: (i) improved transport of intermediate substrate of serial enzymatic reactions and (ii) promotion of the inherent catalytic kinetics of a single enzyme.²⁹ In the former, a charged DNA scaffold is hypothesized to facilitate a substrate transport between two enzymes, so-called substrate channeling that enhances biocatalytic cascade reactions. In this hypothesis, DNA scaffold allows for positioning of enzymes at optimized distances and increasing the flux of the reactive components.^{12, 13, 26} However, previous simulation works showed that the cascade throughput of closely placed enzyme pairs was only enhanced in reactors larger than micron-size cells and for initial time.^{30, 31} Thus, the conflict between the experimental results and

simulated predictions implies that the possible mechanism, substrate channeling, might not be sufficient to explain the activity enhancement.

On the other hand, the second mechanism describes that the local environment of polyanionic DNA materials affects the kinetic constant of single enzyme, such as turnover number and Michaelis constant. It has been hypothesized that a negatively charged DNA surfaces with a high density of phosphate groups could affect the active conformation of an attached enzyme that is surrounded by a strongly bonded hydration layer.²⁷ In order to explain the enhancement of catalytic kinetics of single enzyme, pH profile near DNA surface was modeled and it was concluded that pH might have a critical effect on enzymatic activity.³² Moreover, researches also showed that HRP³³⁻³⁵ and phosphotriesterase^{36, 37}'s activity can be improved by increasing the affinity of substrates on negatively charged DNA motifs, implying that polyanionic DNA material could promote enzymatic activity through altering local chemical and physical micro-environments.

Thus, understanding the mechanisms of how DNA scaffold can modulate the activity of enzymes is of crucial importance. However, the direct effect of polyanionic environments on catalytic kinetics has not yet been experimentally uncovered due to the limitations of conventional colorimetric measurement techniques that are used to monitor reactions.²⁹ Typically, it is quite difficult to measure the catalytic difference of enzymes on the same DNA nanostructures, but at different local environments, due to a lack of assay sensitivity.

In this work, we addressed this challenge by establishing a system that allows probing enzymatic activities over both comparable and distinct polyanionic environments. We used a 3D DNA origami scaffold (OS) of octahedral shape to prescribe GOx either externally at one of the vertices (noted as position A) or, internally, along one of duplex bundles (noted as position B), as illustrated in Figure 1a. The rigid 3D DNA configuration has been previously used to guide the assembly of nanoparticles and biomolecules into 1D, 2D and 3D organizations. We adapted the design and used the OS as a 3D scaffold for targeted GOx placement. The two GOx positions were selected due to the prominently different densities of phosphate groups, as defined by the amount of DNA spatially surrounding the enzyme: position A (a vertex formed by four DNA bundles) > B (on a DNA bundle). The position design allows differentiating two polyanionic environments. Then, an oxidation activity of GOx-OS nanostructure was investigated to reveal an effect of DNA scaffold on a catalytic activity.

We applied a bipolar junction transistor (BJT) based label-free pH sensor to investigate the activity of these two types of GOx-OS nanostructures (Figure 1b). This BJT sensor with high resolution and high sensitivity was recently proposed and validated. 41, 42 It has also been used to study the kinetics of non-specific DNA binding to surfaces.⁴³ Different from the conventional colorimetric or fluorometric methods that require other biocatalysts or derivatizing chemical reagents, this electronic method permits us to directly probe pH/proton concentration changes in aqueous solutions. BJT-based probing offers a limit of detection (LOD) of 0.0003 pH and > 20 times increase in a signal to noise ratio (SNR) over state of the art field effect transistor (FET). 42, 44, 45 The proton concentration changes are resulted from gluconic acid (GA), produced by the GOx-mediated glucose oxidation, because GA is a weak acid and it dissociates over 95% at pH >7. As shown in Figures 1b and S1, the BJT pH sensor is composed of three basic components: (i) a BJT device as the transducer, (ii) a pH-sensitive TiN sensing surface and (iii) a reference electrode; both the sensing surface and the reference electrode are immersed in the studied aqueous solution with GOx-OS. By taking advantage of this sensing approach, we uncovered the difference in enzymatic activity of GOx bound at the different locations of the 3D OS. Our finding indicates that GOx externally placed at a vertex (position A) exhibited a higher activity than GOx anchored on a DNA bundle (position B), which supports the hypothesis of inherent GOx activity enhancement by a negatively charged DNA scaffold. We conclude that it is the resulting local pH decrease associated from the different local DNA organization and topology that favorably affects GOx activity, as we discuss below.

RESULTS AND DISCUSSION

The octahedral DNA scaffold (OS), composed of 12 six-double helix bundles, was fabricated using the DNA origami technique, ^{46, 47} where an M13mp18 single-stranded DNA (ssDNA) was mixed with ~120 staples to form the designated OS structure. ³⁸ To place glucose oxidase (GOx) at designated positions of the OS, a selected vertex (position A) and a placement on the interior position (non-vertex) of a selected bundle (position B) were separately encoded with an extended ssDNA sequence from the staples, known as the "sticky ends", which specifically hybridized with the complementary ssDNA functionalized on GOx (ssDNA-GOx, see Figure 1a, Method and Supplementary Material Part 3).

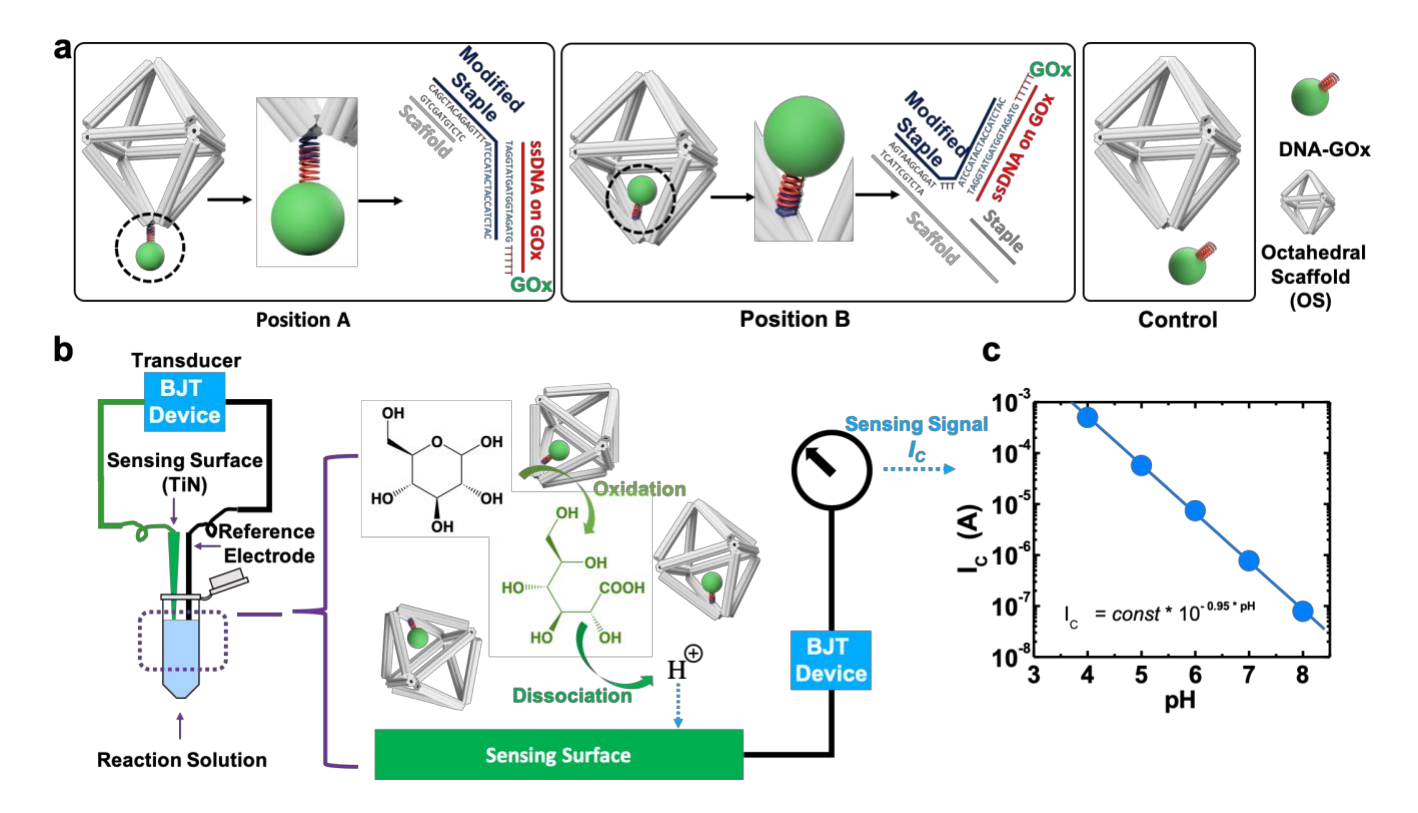


Figure 1. Mechanism for the detection of glucose oxidase (GOx) activity using the bipolar junction transistor (BJT) sensor. (a) Three sets of octahedral DNA scaffold (OS)-GOx conjugates, where the GOx conjugated with single-stranded (ss) DNA is positioned at different locations (external and internal positions A and B, respectively) of the scaffold via DNA hybridization. GOx is represented by a green sphere. (b) Schematic shows the glucose oxidation reaction catalyzed by the OS-GOx. The protons generated during the oxidation process change the pH of the weakly buffered solution which is measured by the BJT-based sensor with collector current (Ic) as the sensing signal. (c) Calibration curve of pH dependence of sensing signal: the sensing current (Ic) is plotted against the pH of the buffer solution, where symbols are measured data and the solid line is a fit to the data.

In our study, the glucose oxidation induced by the GOx-OS architectures took place in diluted TE buffer (2 mM Tris, 0.2 mM EDTA and 12.5 mM MgCl₂, pH=7.35). Diluted Tris and EDTA served as buffering components to mildly maintain a starting pH value. As discussed in the Supplementary Material (Part 1c), we also investigated the effect of buffer capacity on GOx reactions for the BJT measurement, where different concentrations of the Tris buffers were used. The conclusion is that a strong buffer can impair the BJT measurement due to the buffering effect on neutralizing proton changes (Figure S5 and S6), while a weak buffer can decrease a GOx

activity because its inability of maintaining a proper and stable environment for enzymatic reaction (Figure S7). We also modelled the effect of buffer capacity on electrostatic environment near DNA nanostructures (Supplementary Material, Part 1g), and the computations indicate that diluted buffer could show a larger variation of pH near a DNA surface relatively to the bulk (Figure S12). Therefore, a diluted TE buffer is the most suitable, and it has been used in this study. The concentration of magnesium ions (Mg²⁺) in all the buffers was kept at 12.5 mM in order to stabilize the OS structure by preventing inter-DNA repulsions between the negatively charged phosphate backbones.

To evaluate the catalytic properties of the GOx-OS nanostructures in the presence of glucose, the BJT pH sensor was applied to measure the sensing current (Ic) in response to changes in the pH of the solution due to the enzymatic reaction. Figure 1c shows the pH calibration curve for the BJT sensor with the collector current Ic as the sensing signal. The sensing signal (Ic) dependence was measured as a function of various pH buffer solutions at room temperature and fixed applied voltages; symbols are the measurements and solid line is fit to the data. From the fit (Figure 1c), the measured dependence of Ic on pH can be presented as:

$$I_C = \kappa \cdot 10^{-\alpha \cdot pH} \, (1)$$

where $\alpha = 0.95$ and κ is constant.

Since an addition of glucose to the GOx solution for triggering enzymatic reaction results in pH change, the relationship between measured signal I_C (t) and solution pH(t) at time t after the glucose addition can be written as:

$$\frac{I_c(t)}{I_0} = 10^{-0.95(pH(t) - pH(0))}$$
 (2)

where I_0 and pH(0) are collector current I_C and solution pH prior to the glucose addition.

We applied this BJT sensor to probe the catalytic reactions of GOx-OS systems with two different GOx locations, as described above. To verify whether the BJT sensor could distinguish subtle differences in proton generation among different GOx-OS systems, three GOx-OS sets were designed: control, position A and position B (Figure 1a). The control experiment served to examine activity changes due to the presence of DNA scaffolds, and thus the solution contained free

ssDNA-GOx conjugates and OS without encoded sticky ends. As shown in Figures 2a-c, the OS and GOx-OS structures are clearly visible in the negative-stained micrographs obtained by transmission electron microscopy (TEM). Since GOx is a dimeric globular protein with dimensions of 6.0×5.2×7.7 nm,⁴⁸ the enzyme is presented as the faint globular objects positioned externally and internally on the OS (Figures 2b-c, as indicated by yellow arrows). We estimated the yields of GOx placement at the positions A (48%) and B (51%) based on TEM imaging and analysis of 207 and 224 counted OS structures, respectively. It is noteworthy that in order to prepare GOx-OS samples, we mixed ssDNA-GOx and OS in a molar ratio of 1:1.2 (ssDNA-GOx: OS). Thus, the statistic results of GOx-OS yields show that the actual concentration of well-formed GOx-OS, unbound ssDNA-GOx and unfunctionalized OS were close in the samples GOx-OS (A) and (B). Therefore, our study on activity comparison between GOx-OS(A) and (B) is based on a similar concentration of GOx.

We first used the BJT sensor to explore the three GOx-OS systems (control, and with target enzyme at the positions A and B, denoted as GOx-OS(A) and GOx-OS(B)) and compared real-time I_C in the absence and presence of glucose. Here, glucose is required as a substrate for the enzymatic reaction. Figures 2d-f show the real-time monitoring data of working curves, $I_C(t)$, in these three systems before and after adding glucose in diluted TE buffer. Before adding glucose (blue curve), the current flows remained flat, exhibiting negligible fluctuations of pH. It is worth noting that the absolute I_C in the absence of glucose varied due to the initial pH variations: pH = 7.39 for a control set, pH = 7.35 for GOx-OS(A), and pH = 7.42 for GOx-OS(B) as measured by a benchtop pH meter. After adding glucose (Figures 2d-f, orange curves), the change of I_C behavior indicated proton generation. Note that the higher I_C at t = 0 s after the addition of glucose (orange curves), compared to the baseline (without glucose, blue curves), was due to the spontaneous oxidation of glucose to gluconic acid before dissolution and a necessary manual operation before starting the measurements (approximately 30 s).

The real-time current monitoring (Figures 2d-f) clearly shows the process of buffering glucose oxidation reaction: (i) during the initial time (0 to 100 s), the rate of I_C increase grew because of buffering disequilibrium; then (ii) in a steady state (100 to 200 s), the rate of I_C increase remained steady. We note that the unsteady state (i) was different from conventional enzymatic kinetics that displays initially a linear rate. The unsteady state resulted from the pH fluctuation caused by substrate addition at the early reaction time. This state was detected by the BJT-based pH sensor,

but not the conventional colorimetric methods. Such a behavior of steady state (ii) may occur since after the pH fluctuation the dissociation reaction of GA produced from the oxidation reached an equilibrium with the buffering process, stabilizing I_C increase. Thus, the real-time monitor of I_C reveals a two-stage process, indicating a high sensitivity of this type of pH measurement. These apparent differences in the oxidation reaction process, as monitored by the BJT sensor, were used for the detailed investigation of the effect of enzyme positioning on the 3D DNA scaffold, as we discuss below.

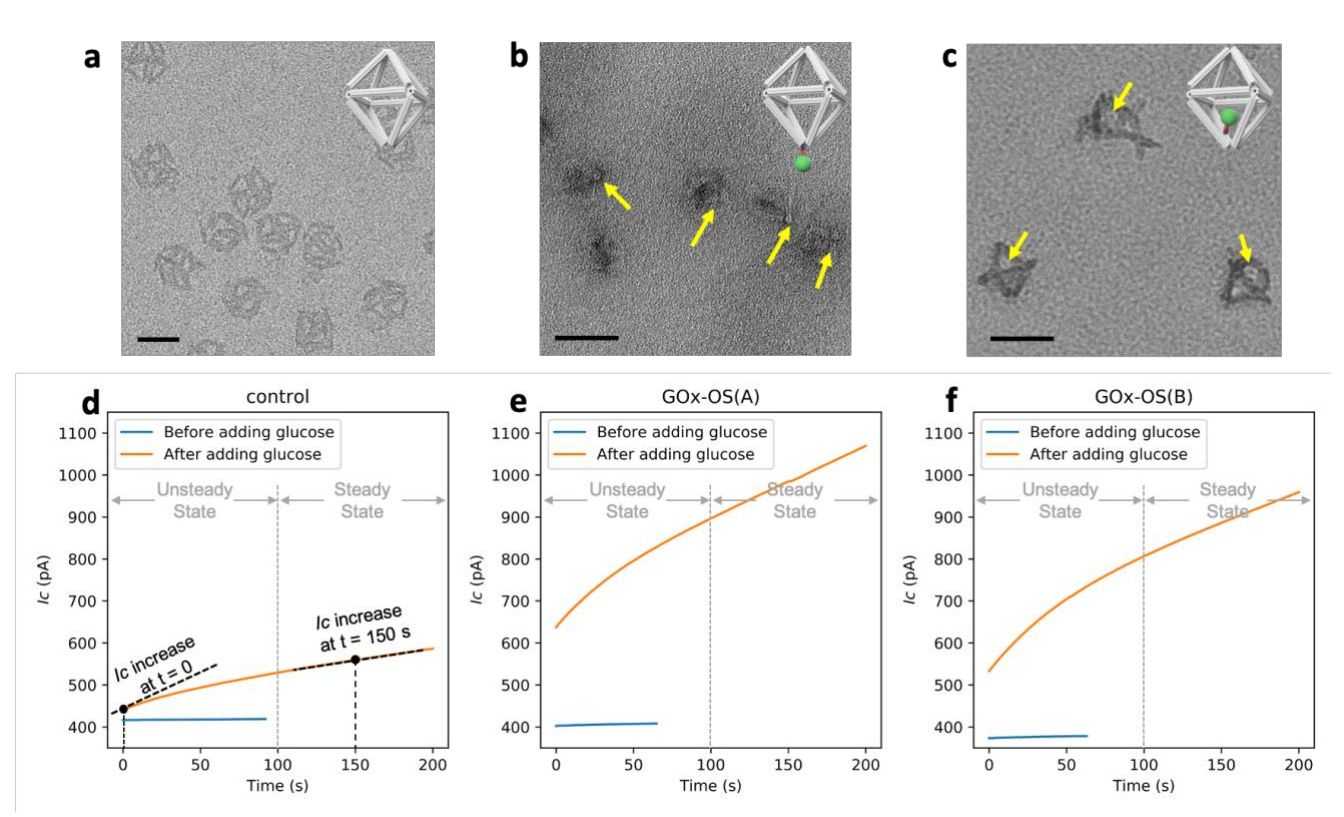


Figure 2. Structure of GOx-OS architectures and temporal dependence of BJT-sensing current (I_c).

TEM images of (a) octahedral DNA scaffold (OS), (b) GOx-OS(A), (c) GOx-OS(B). In (b) and (c), GOx is indicated by yellow arrows. (d-f) Time dependence of I_C before and after glucose addition, as monitored by the BJT sensor. Blue curve shows I_C before adding glucose. The solution contained 0.4 nM of ssDNA-GOx (control) or GOx-OS. Orange curve shows a current flow after adding glucose. Compared to the blue and orange curves, uprush at 0 s resulted from glucose addition and oxidation reaction when setting the transistor probe. During the unsteady state (0 to 100 s), the rate of I_C increase went up because of turbulence disruption caused by adding glucose. In the equilibrium stage (100 to 200s), the rate of I_C increase maintained consistent (scale bars: 50 nm).

Next, we quantified a time evolution of proton concentration by accounting proton concentration ($[H^+(t)]$) dependence on $I_C(t)/I_0$. Since $pH(t) = -\log_{10}([H^+(t)])$ with $[H^+(t)]$ as the corresponding proton concentration of the measured solution, the above Equation (2) can be rewritten as:

$$[H^{+}(t)] = [H_0^{+}] \left(\frac{I_c(t)}{I_0}\right)^{\frac{1}{0.95}} = [H_0^{+}] \left(\frac{I_c(t)}{I_0}\right)^{1.05}$$
(3)

Using the data presented in Figure 2d-f and Equation (3), we show in Figure 3a the time dependence of proton accumulation ($\Delta[H^+(t)] = [H^+(t)] - [H_0^+]$). Here, the three measurements (groups 1-3) correspond to three batches of GOx-OS preparations. Although a pH adjustment of different batches contributed to discrepancies in absolute proton accumulation of the groups, similar trends among the three GOx-OS systems were observed: (i) the rate $\Delta[H^+(t)]$ in control system was lower than for the two GOx-OS ones, indicating that the enzymatic activity of GOx was enhanced by the DNA scaffold and leading to a boosted proton generation; (ii) $\Delta[H^+(t)]$ for GOx-OS(A) (orange curve) was consistently higher than for GOx-OS(B) (green curve) in each group, implying that GOx at position A had a higher enzymatic activity than GOx at position B. This result suggests that enzyme location on the OS affects its catalytic property.

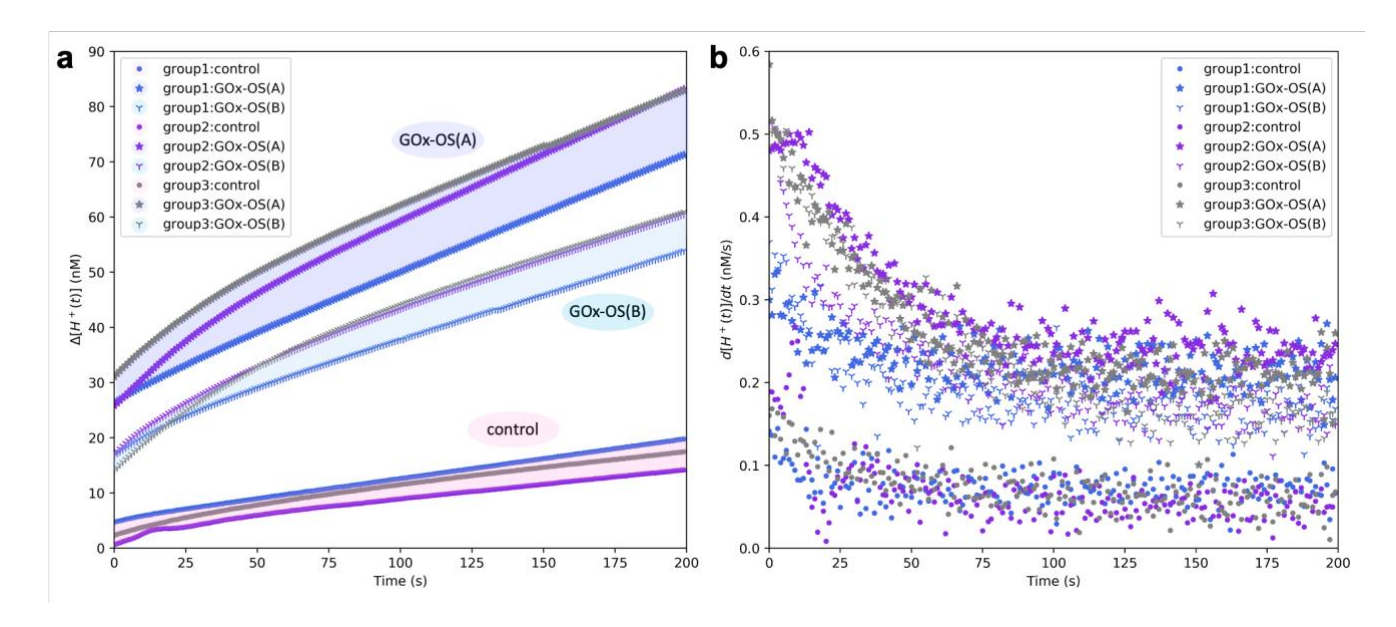


Figure 3. Real-time monitoring of proton accumulation $(\Delta[H^+(t)] = [H^+(t)] - [H_0^+])$ and proton generation rate $(\frac{d[H^+(t)]}{dt})$ by the BJT sensor. Changes of $\Delta[H^+(t)]$ (a) and $\frac{d[H^+(t)]}{dt}$ (b) within 200 s were monitored in diluted TE buffer upon glucose addition, where three independent experiments (groups 1, 2 and 3) were performed, respectively. Samples in different groups correspond to different preparation batches. Blue, orange and green curves correspond to the control, GOx-OS(A) and GOx-OS(B) systems respectively.

In order to further study the catalytic activity of GOx-OS systems, we compared the proton generation rate $(\frac{d[H^+(t)]}{dt})$ of the three designed sets. Based on equation (3), the proton accumulation over time is shown below:

$$\frac{d[H^+(t)]}{dt} = 1.05 \frac{\left[H_0^+\right]}{I_0^{1.05}} I_c(t)^{0.05} \cdot \frac{dI_c(t)}{dt} \text{ or } \frac{d[H^+(t)]}{dt} = \frac{[H^+(t+\Delta t)] - [H^+(t)]}{\Delta t} (4)$$

According to Equation (4) and the initial pH of three sets (Figures 2d-f, blue curve as baseline), we can convert an electronic signal to $\frac{d[H^+(t)]}{dt}$ by setting $\Delta t = 1 \, s$. As Figure 3b shows, an unsteady regime of $\frac{d[H^+(t)]}{dt}$ was observed in the first 100 s, upon glucose addition. We propose that this regime can be attributed to a buffering effect. In particular, the pH reduction by glucose addition could result in a temporary non-equilibrated situation. Such an effect was confirmed by adding the same amount of glucose to buffer in the absence of GOx-OS, where the voltage applied at the emitter (V_E) can also be utilized to probe pH change and a negative correlation between the V_E and I_C was observed. As shown in Figure S9, V_E quickly jumped down after 30 s after setup, then it slowly went back with a negative acceleration in rate. Eventually, V_E did not return to the initial value. The stable V_E after glucose addition was lower than the initial V_E , implying the presence of a more acidic environment due to the addition of glucose. Therefore, glucose can induce a negative acceleration in the rate of V_E , which in turn, contributed to the unstable behavior of proton generation during the initial reaction period from 0 to 100 s. In the steady state (100 to 200 s), the reaction achieved the equilibrium among glucose oxidation, dissociation of GA and buffering. Therefore, we can estimate the enzymatic activity by comparing $\frac{d[H^+(t)]}{dt}$ in steady state: GOx-OS systems performed better than free GOx control set in producing protons. GOx-OS(A) showed a higher reaction rate than GOx-OS(B).

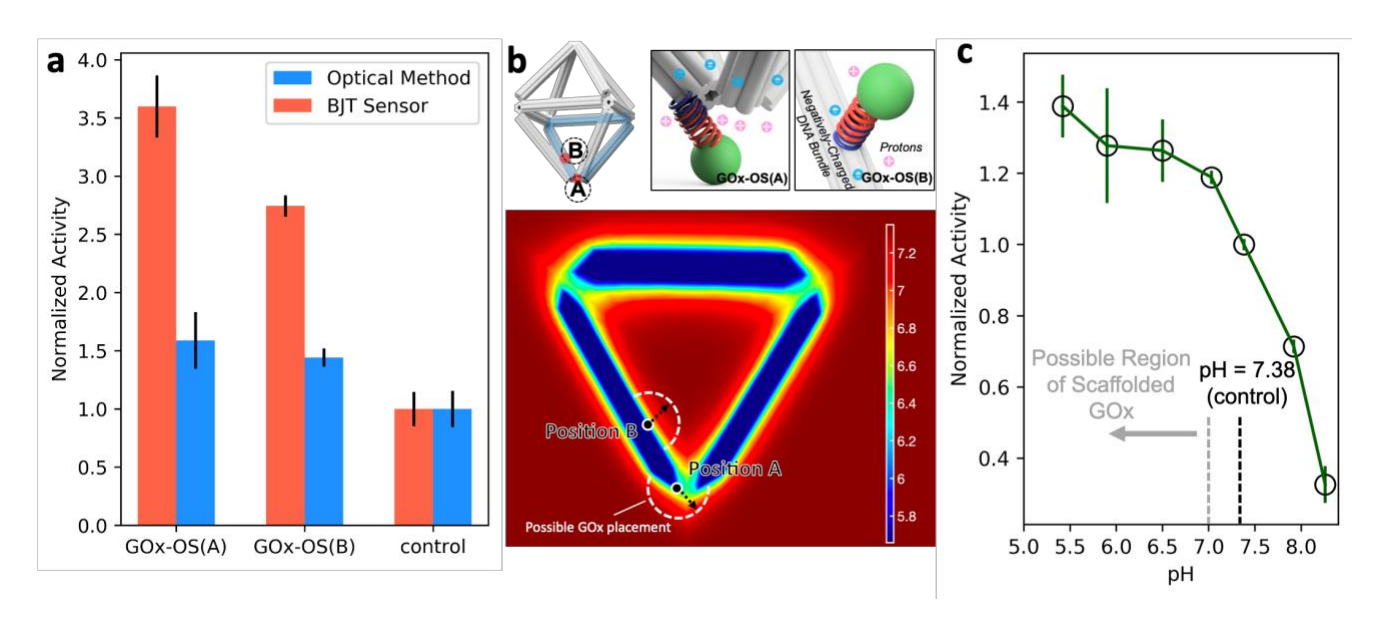


Figure 4. Proposed mechanism of activity difference among three GOx-OS systems. (a) Comparison between electronic (BJT-based) and optical characterization of GOx activity (0.4 nM GOx-OS nanostructures): Normalized enzymatic activity of three independent GOx-OS sets in diluted TE buffer, as measured by the BJT sensor (red) and optical method (blue). BJT sensor data (Figure 3) were analyzed using Equation (4) by averaging $\frac{d[H^+(t)]}{dt}$ in a range of 100 s to 200 s. Optical data is obtained by UV-Vis spectroscopy as discussed in the text, respectively. All activities are normalized to the enzymatic activity of control sets measured by the corresponding methods. (b) Scheme and modelling of negatively charged DNA bundles and vertex contributing to the local pH environment of GOx, where three bundles labeled in blue were selected for simulating pH map (see Supporting Material for details). The color-coded pH scale ranges from the highest pH (pH=7.38), red, to lowest pH=5.67, blue. (c) pH-activity profile of ssDNA-GOx in diluted TE buffer (averaged for three measurements) as probed by optical method (2 nM ssDNA-GOx). All activities are normalized to the activity at pH = 7.38.

In Figure 4a, we summarize an average proton generation rate during steady regime, from 100 s to 200 s, as shown in Figure 3. It is noteworthy that the BJT probing integrates the reaction-produced protons and the buffer-consumed protons. The data in unsteady state (0 - 100 s) is closer to the real enzymatic reaction than in steady state (100 - 200 s) due to the lower buffering effect at the initial stage of the reaction. However, the dependences of the interpretation on the initiation time and decay at this stage make the proton generation rate estimation difficult. Thus, we use a steady state regime for comparing GOx activity. We note that while in this regime a lower activity is expected due to a discussed buffering effect, such measurements are more reliable for cross-comparisons. Red bars in Figure 4a display the normalized GOx activities of GOx-OS(A), GOx-OS(B) and control systems by the BJT sensor.

The findings show that the enzyme at position A (at the vertex) is about 25-30% more active than at position B (at the edge), while both GOx-OS sets are 2 to 3.5 times more active than the control sets (unbound enzyme). In order to compare the BJT-based sensing results with those for the conventional optical method, we examined the enzymatic activity of all studied systems using a 2,2'-azino-bis(3-ethylbenzothiazoline-6-sulfonic acid) (ABTS) assay. This assay probes a kinetics of hydrogen peroxide (H_2O_2), which is a product of glucose oxidation reaction, and the results are shown by blue bars in Figure 4a (see Method). The optical measurements indicate that the enzymes attached to OS exhibited enhanced activity. However, they are unable to differentiate between two GOx-OS positions. In contrast, the high resolution ($\Delta pH \sim 0.0003$)⁴⁴ of the BJT pH sensor is readily able to resolve small difference in enzyme activities associated with the two GOx-OS positions. Intrinsically different mechanisms for sensing, a one-step reaction for the measuring of protons for BJT vs a two-step reaction for the measuring of H_2O_2 for ABTS assay, might be responsible for enhanced sensitivity by electronic method. Thus, both electronic and optical sensing methods show an enhanced activity of the enzyme on DNA scaffold, but only an electronic method can resolve dependence of the enzyme activity on its location on a 3D DNA scaffold.

It has been reported that electrostatic interaction between enzymes and carriers can affect apparent enzymatic activities.⁴ For example, ionic-liquid-coated lipase in organic solvent was observed to enhance activity because of the micro-partition of water attracted by the ionic liquid.⁴⁹ Besides, many studies demonstrated that GOx coated on positively-charged polymers or metal surfaces, widely used for bio-sensor fabrications, displayed the enhancement of enzymatic solubility and stability due to the electrostatic interactions with carriers.^{50, 51} Thus, based on our

experimental results, we propose that the negatively charged DNA scaffold, the GOx's carrier, enhances enzymatic catalysis by creating an electrostatic micro-environment, specifically, by increasing a local pH (Figure 4b). The phosphate backbones of DNA, by attracting protons, lead to a higher acidity of local environment surrounding GOx. The magnitude of the effect might depend on the details of local arrangements of negatively-charged DNA backbones. In our case, since GOx at the position A is attached to the vertex of four six-double helix bundles, it experiences a higher amount of DNA in its proximity, in comparison with GOx at position B, which is placed on one six-double helix bundle. This larger amount of DNA backbones surrounding GOx can result in a more acidic local environment. Since the intrinsic GOx activity is increased with acidity, lower local pH can consequently boost an enzymatic activity of GOx-OS(A) over GOx-OS(B).

To model a local pH at position A and B, we selected three bundles (blue bundles in Figure 4b) and computed the pH map based on *Poisson-Boltzmann equation* and *Boltzmann distribution*. Using *Debye-Hückel approximation* to simplify the *Poisson-Boltzmann equation*, we obtained the following equation for spatial electric potential ψ with boundary conditions:

$$\nabla^2 \psi = \kappa^2 \psi \quad (5)$$

$$\psi(DNA \ surface) = \psi_0$$

$$\psi(bulk \ solution) = 0$$

where $\lambda_D = 1/\kappa$ is the Debye length. We estimated $\lambda_D = 2 nm$ in our diluted TE buffer and $\psi_0 = -100 \, mV$ from the Grahame's Equation (see Supplementary Material, Part 1g).

The relationship between electric potential and local pH is given as the following from *Boltzmann distribution*:

$$pH = pH_0 + \frac{F\psi}{2.3 \ RT} \ (6)$$

where pH_0 is the pH at bulk solution, R is the universal gas constant, and F is the Faraday constant. Thus, using Equation (5) and (6) and $pH_0 = 7.38$ (GOx at control set exposed to the same pH), we calculated the pH map of the three selected bundles, representing an octahedral face, with 5 nm diameter and 30 nm length.

Next, the distance of GOx to OS was estimated by approximating the ssDNA sequence of DNA linker to Gaussian Model and dsDNA bases to rigid-rod model⁵²:

$$< R_{bridge}^2 > = 2l_p \sigma L_{ss} + \sigma_{ds}^2 d_i^2$$
 (7)

where $\langle R_{bridge}^2 \rangle$ is the mean square end-to-end distance of the DNA linker connecting GOx and OS, l_p is a persistence length of ssDNA, σ is the length per base in ssDNA, L_{ss} is the ssDNA bases in total, σ_{ds}^2 is the square of the length per base pair in dsDNA, d_i^2 is the square of the dsDNA bases in total. Our DNA linker was composed of 5 ssDNA bases and 18 dsDNA base pairs and thus the distance of GOx to OS was estimated as 6.5 nm.

Figure 4b, pH map displays the local pH around three bundles, where the binding sites of OS(A) and (B) are shown by black circles and the possible location of linked GOx is marked by white dash line at 6.5 nm from the binding site. The calculated pH map with three selected bundles indicates that the local environment of position A is affected much greater than position B.

Based on this explanation, we then experimentally estimated the effect of local pH environment on GOx activity in the reaction buffer. We first determined the pH dependence of ssDNA-GOx activity using a commonly used optical method (Figure 4c) based on the ABTS assay, as discussed above, because this approach provides a well-established methodology that can be applied to our studies. The comparison between GOx-OS activity (Figure 4a) and the referenced pH-activity profile (Figure 4c) supports our hypothesis of acidic micro-environment near DNA construct. Indeed, in Figure 4a, optical probing (blue bars) for GOx-OS(A) and GOx-OS(B) systems show 40-50% higher activity than a control set. Meanwhile, for bulk measurements of ssDNA-GOx (Figure 4c), about 40% activity enhancement over the bulk TE solution (pH = 7.38) is observed at acidic solution (pH < 7.0). The two comparable activity trends suggest that the OS could create a local environment for GOx with a pH lower than 7.0. As evident from pH-activity profile, a negligible difference of GOx activity is observed by optical method at a pH range of 5.5 to 7.0 (Figure 4c). This phenomenon may result in inability of optical method to differentiate GOx activities at two positions, GOx-OS(A) and GOx-OS(B). On the contrary, the BJT sensor reliably differentiates that GOx-OS(A) is 25-30% more active than GOx-OS(B), as discussed above. Thus, we conclude that the presented electronic sensing method reveals the dependence of enzymatic activity on the micro-partitioning of ions due to DNA nanostructure, the effect that was proposed but was not yet proven by other studies.^{29, 32, 53} We note that in addition to the leading effect of ionic micro-partitioning observed here, hydration shell²⁶ might play a role in the modification of enzymatic activity.

CONCLUSIONS

In summary, we show an electronic method for sensing enzymatic activity of GOx-mediated glucose oxidation reactions using a bipolar junction transistor (BJT). We used a 3D DNA octahedral scaffold (OS) as a carrier for GOx, and the enzymatic activities in the GOx-OS systems were directly measured by the BJT device, a label-free pH sensor. This transistor sensor exhibits a higher resolution for detecting proton generation rate than conventional optical methods in the condition of a slow reaction. Our study reveals that the GOx-OS systems showed a higher catalytic oxidation rate than free GOx in solution. Interestingly, using this BJT-based method we found that GOx placed at one vertex of the DNA octahedra performed a faster oxidation rate than embedded between the bundles of the OS edge. We relate this effect to different local pH environments induced by the OS due to exposure of GOx to different amounts of negatively charged DNA scaffold. The phenomenon results in electrostatic micro-partitioning of protons around the active sites of enzymes. The difference of local environments caused by DNA density, in turn, can accordingly influence enzymatic activity because of the demonstrated relationship between enzymatic catalysis and pH. Therefore, enzymes scaffolded at different locations are immersed into distinctive micro-environments, thus displaying different catalytic properties.

METHODS

Synthesis and Purification of DNA scaffold. Octahedral DNA scaffold (OS) was made from mixing 100 nM of each of total 144 staples oligonucleotides, 20 nM M13mp18 scaffold and buffer solution. Buffer solution was composed of 1 mM EDTA, 12.5 mM MgCl₂, and 5 mM Tris buffer (pH = 7.9 at 20 °C). The mixed solution above was then aliquoted to 100 μ L in PCR tubes and put into a PCR thermocycler, which annealed the solution and led to DNA self-folding process. The program of the PCR thermocycler rapidly heated the solution to 90 °C in 5 min, then slowly cooled down to 61 °C over 80 min, followed by slow cooling from 60 °C to 4 °C in the end. The total annealing time was about 20 hours. These annealed origami samples were then gel-purified to remove the excess of unfolding staples and scaffolds.

Agarose gel electrophoresis was conducted to purify the origami samples. Agarose gel (1 wt%) in 0.5X TBE and 10 mM MgCl₂ was heated in the microwave and then mixed with 10.5 µg/ml Syber Gold nucleic acid gel stain. After solidifying at room temperature, the gel was immersed in the same buffer. Samples were mixed with a gel loading dye and carefully loaded into the gel.

Electrophoresis was performed at 65 V for 2.5 h at room temperature. Targeted bands were monitored under ultraviolet light and the purified samples were extracted using a gel extraction (cellulose-acetate) column and centrifuged for 10 min at 2,000 rcf.

After purification, the concentration of origami solution was confirmed by NanoDrop microvolume spectrophotometer (Thermo Scientific NanoDropTM Lite Spectrophotometer) with a ratio of 0.25 nM μ L/mg. Then we roughly adjusted the pH of origami solution to 7.5 by adding HCl and stored them at 4 °C.

Functionalization of Glucose Oxidase. Glucose oxidase (GOx, Sigma Aldrich) in PBS buffer was first mixed with N-ε-maleimidocaproyl-oxysulfosuccinimide ester (sulfo-EMCS) at a ratio of 1:20 for 1 h at room temperature, and then purified by a Zeba desalting column (40k MWCO 0.5 mL). Thiolated oligonucleotides (IDT) were first reduced by tris(2-carboxyethyl)phosphine (TCEP) at a ratio of 1:1000 in PBS buffer and the excess TCEP was removed by a size exclusion column (G-25, GE Healthcare). Next, the sulfo-EMCS-treated enzymes were mixed with the activated oligonucleotides at a ratio of 1:8 in PBS buffer and incubated at room temperature overnight. The DNA-attached enzymes were then purified by an Amicon cutoff filter (50k). The number of DNA attachment on enzymes was quantified by UV-Vis by the following. Figure S2 shows an example of the DNA-attached GOx:

$$\begin{split} A_{260}(\text{conjugates}) &= \epsilon_{260}(\text{DNA})\text{C}(\text{DNA}) + \epsilon_{260}(\text{GOx})\text{C}(\text{GOx}) \\ A_{452}(\text{conjugates}) &= \epsilon_{452}(\text{GOx})\text{C}(\text{GOx}) \end{split}$$

In our study, the number of DNA attached to enzymes was: 1.0 for GOx.

In order to confirm DNA-GOx conjugates, we performed agarose gel electrophoresis (1wt%, in 1X TBE) with Syber Gold nucleic acid stain. As Figure S3 shows, DNA-GOx conjugates moved slower than free DNA and only one visible band stained by Syber Gold was detected, which proved that most of the GOx were functionalized with DNA.

Sample Preparation and Sensing Process. Prior to electronic measurement, we firstly incubated OS and GOx together overnight with a ratio of 1.2 OS to 1 GOx to generate the OS-GOx conjugate. Then we prepared 0.4 nM OS-GOx in the working solution containing weak Tris buffer. Before adding glucose, we immersed the sensor probe and electrode into 1168 μ L working solution to collect sensor signal in I_C as a reference. Next, 32 μ L glucose solution was added to the working

solution to achieve 80 mM glucose for enzymatic reaction. After \sim 30 s for mixing and probe setup, we started to record sensing signal, I_C .

GOx Activity Measurements *via* Horseradish Peroxidase (HRP)/ABTS Assay. Glucose Oxidase (GOx) and HRP are two catalysts for two independent reactions. In particular, when glucose reacts with oxygen under GOx catalytic reaction, it produces D-glucono-δ-lactone and hydrogen peroxide. The product, hydrogen peroxide, from GOx catalytic reaction can react with 2,2'-azino-bis(3-ethylbenzothiazoline-6-sulfonic acid) (ABTS) under HRP catalytic reaction to form ABTS radical cation (ABTS*+). Thus, GOx and HRP interact as a cascading reaction. ABTS*+ is a reaction signal with an absorbance maximum at 415 nm in ABTS assay, which can be measured by ultraviolet-visible spectroscopy (UV-Vis, Cary 300).

In our experiment, samples were prepared one night beforehand. First, OS solution was diluted to 3 nM and pH was corrected to pH = 7.5. The DNA functionalized GOx had a stock concentration of 241 nM and was diluted by the weak buffer to 24.1 nM. Then 24 μ L diluted OS, 2.8 μ L diluted functionalized GOx, and 53.2 μ L buffer were mixed together to form the sample solution and incubated at room temperature for 14 hours.

For the optical measurement, UV-Vis was warmed up for half an hour and the absorbance wavelength was set to 415 nm. In a typical experiment, the following working solution was mixed and added into the cuvette and measured immediately. The working solution contained 35.3 μ L ABTS (17 nM), 1.81 μ L HRP (166 μ M), 71.2 μ L sample prepared overnight, 8 μ L glucose (3 M), and buffer was added to a total volume of 300 μ L. The above recipe was for 80 mM glucose with 0.4 nM OS-GOx measurement, and the amount of buffer added was adjusted accordingly when measuring different glucose concentrations. Figure 9S shows the dependence of reaction rate on glucose concentration using ABTS assay.

ASSOCIATED CONTENT Supporting Information

The Supporting Information is available free of charge on the ACS Publications website at DOI: xxx.

Synthesis and purification of octahedral DNA scaffold (OS); Functionalization of glucose oxidase (GOx); Comparisons of oxidation reaction among weak buffers; Dependence of pH change on proton generation using the BJT sensor; Blank control of glucose addition using the BJT sensor; GOx activity measurements *via* horseradish peroxidase (HRP)/ABTS assay; Models of pH-distance profile near DNA origami; Sample preparation and transmission electron microscopy; Octahedral scaffold; DNA strands for GOx-OS attachment (PDF)

ACKNOWLEDGEMENT

The work was supported by the National Science Foundation under Grant No 1905920. The DNA design work was supported by the US Department of Energy, Office of Basic Energy Sciences, Grant DE-SC0008772. This research used resources of the Center for Functional Nanomaterials, supported by U.S. DOE Office of Science Facilities at Brookhaven National Laboratory under Contract No. DE-SC0012704. We would like to acknowledge the Imaging Facility of CUNY Advanced Science Research Center for instrument use, scientific and technical assistance. We thank Zhe Yuan for help with modeling of pH map and Dr. Jason Kahn for helpful discussions.

AUTHOR INFORMATION

Y.X., S.Z. and O.G. conceived the idea. Y.X. and S.Z. conducted and designed the experiments. Y.X. and O.G. wrote the paper. J.H. helped with optical measurement. S.W. contributed to the electron microscopy characterization. S.Z. and O.G. supervised this project. All authors discussed the results and commented on the manuscript. The authors declare no competing interests.

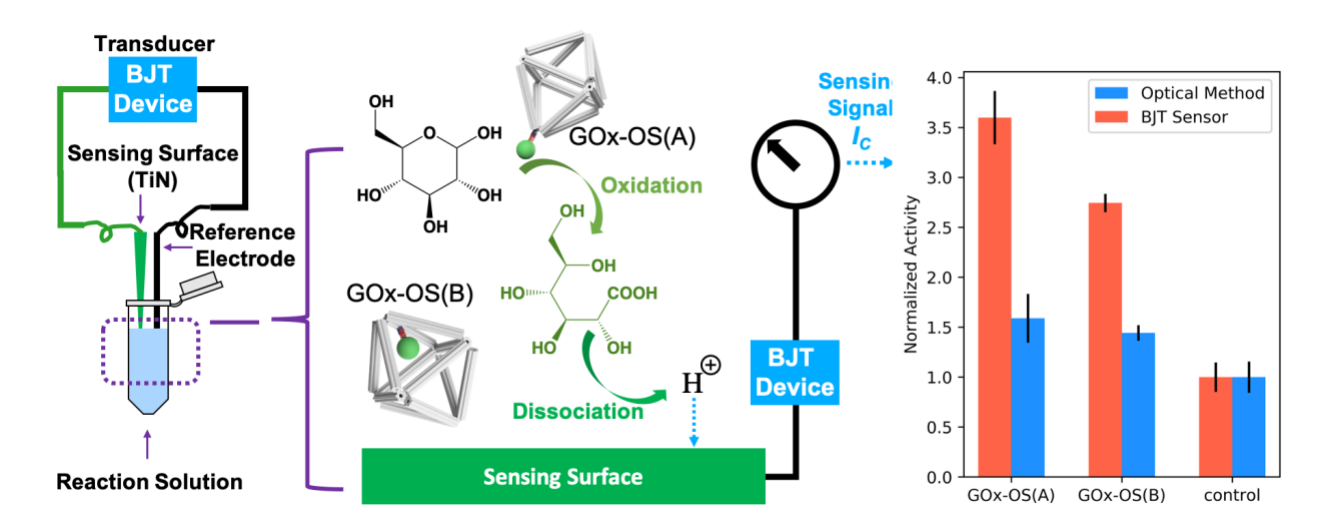
REFERENCES

- 1. Kuchler, A.; Yoshimoto, M.; Luginbuhl, S.; Mavelli, F.; Walde, P., Enzymatic Reactions in Confined Environments. *Nat Nanotechnol* **2016**, *11*, 409-420.
- 2. Ariga, K.; Ji, Q.; Mori, T.; Naito, M.; Yamauchi, Y.; Abe, H.; Hill, J. P., Enzyme Nanoarchitectonics: Organization and Device Application. *Chem Soc Rev* **2013**, *42*, 6322-4635.
- 3. Vázquez-González, M.; Wang, C.; Willner, I., Biocatalytic Cascades Operating on Macromolecular Scaffolds and in Confined Environments. *Nat Catal* **2020,** *3*, 256-273.
- 4. Zhang, Y.; Ge, J.; Liu, Z., Enhanced Activity of Immobilized or Chemically Modified Enzymes. *ACS Catal* **2015**, *5*, 4503-4513.

- 5. Schoffelen, S.; van Hest, J. C., Chemical Approaches for the Construction of Multi-Enzyme Reaction Systems. *Curr Opin Struct Biol* **2013**, *23*, 613-621.
- 6. Ansari, S. A.; Husain, Q., Potential Applications of Enzymes Immobilized on/in Nano Materials: A Review. *Biotechnol Adv* **2012**, *30*, 512-523.
- 7. Lian, X.; Fang, Y.; Joseph, E.; Wang, Q.; Li, J.; Banerjee, S.; Lollar, C.; Wang, X.; Zhou, H. C., Enzyme-MOF (Metal-Organic Framework) Composites. *Chem Soc Rev* **2017**, *46*, 3386-3401.
- 8. Filipov, Y.; Zakharchenko, A.; Minko, S.; Katz, E., Magneto-Controlled Biocatalytic Cascades with Logically Processed Input Signals Substrate Channeling *versus* Free Diffusion. *Chemphyschem* **2018**, *19*, 3035-3043.
- 9. Ellis, G. A.; Klein, W. P.; Lasarte-Aragonés, G.; Thakur, M.; Walper, S. A.; Medintz, I. L., Artificial Multienzyme Scaffolds: Pursuing *In Vitro* Substrate Channeling with an Overview of Current Progress. *ACS Catal* **2019**, *9*, 10812-10869.
- 10. Linko, V.; Nummelin, S.; Aarnos, L.; Tapio, K.; Toppari, J. J.; Kostiainen, M. A., DNA-Based Enzyme Reactors and Systems. *Nanomaterials (Basel)* **2016**, *6*, 139.
- 11. Fu, J.; Yang, Y. R.; Dhakal, S.; Zhao, Z.; Liu, M.; Zhang, T.; Walter, N. G.; Yan, H., Assembly of Multienzyme Complexes on DNA Nanostructures. *Nat Protoc* **2016**, *11*, 2243-2273.
- 12. Wilner, O. I.; Weizmann, Y.; Gill, R.; Lioubashevski, O.; Freeman, R.; Willner, I., Enzyme Cascades Activated on Topologically Programmed DNA Scaffolds. *Nat Nanotechnol* **2009**, *4*, 249-254.
- 13. Zhen-Gang Wang, O. I. W., and Itamar Willner, Self-Assembly of Aptamer-Circular DNA Nanostructures for Controlled Biocatalysis. *Nano Lett* **2009**, *9*, 4098-4102.
- 14. Matthies, M.; Agarwal, N. P.; Poppleton, E.; Joshi, F. M.; Sulc, P.; Schmidt, T. L., Triangulated Wireframe Structures Assembled Using Single-Stranded DNA Tiles. *ACS Nano* **2019**, *13*, 1839-1848.
- 15. Nykypanchuk, D.; Maye, M. M.; van der Lelie, D.; Gang, O., DNA-Guided Crystallization of Colloidal Nanoparticles. *Nature* **2008**, *451*, 549-552.
- 16. Park, S. Y.; Lytton-Jean, A. K.; Lee, B.; Weigand, S.; Schatz, G. C.; Mirkin, C. A., DNA-Programmable Nanoparticle Crystallization. *Nature* **2008**, *451*, 553-556.
- 17. Lu, F.; Yager, K. G.; Zhang, Y.; Xin, H.; Gang, O., Superlattices Assembled through Shape-Induced Directional Binding. *Nat Commun* **2015**, *6*, 6912.
- 18. Maye, M. M.; Nykypanchuk, D.; Cuisinier, M.; van der Lelie, D.; Gang, O., Stepwise Surface Encoding for High-Throughput Assembly of Nanoclusters. *Nat Mater* **2009**, *8*, 388-391.
- 19. Wenyan Liu, M. T., Huolin L. Xin, Tong Wang, Hamed Emamy,; Huilin Li, K. G. Y., Francis W. Starr, Alexei V. Tkachenko, Oleg Gang, Diamond Family of Nanoparticle Superlattices. *Science* **2016**, *351*, 6273.
- 20. Aktas, G. B.; Skouridou, V.; Masip, L., Nucleic Acid Sensing with Enzyme-DNA Binding Protein Conjugates Cascade and Simple DNA Nanostructures. *Anal Bioanal Chem* **2017**, *409*, 3623-3632.
- 21. Fu, Y.; Zeng, D.; Chao, J.; Jin, Y.; Zhang, Z.; Liu, H.; Li, D.; Ma, H.; Huang, Q.; Gothelf, K. V.; Fan, C., Single-Step Rapid Assembly of DNA Origami Nanostructures for Addressable Nanoscale Bioreactors. *J Am Chem Soc* **2013**, *135*, 696-702.
- 22. Grossi, G.; Dalgaard Ebbesen Jepsen, M.; Kjems, J.; Andersen, E. S., Control of Enzyme Reactions by a Reconfigurable DNA Nanovault. *Nat Commun* **2017**, *8*, 992.

- 23. Ngo, T. A.; Nakata, E.; Saimura, M.; Morii, T., Spatially Organized Enzymes Drive Cofactor-Coupled Cascade Reactions. *J Am Chem Soc* **2016**, *138*, 3012-3021.
- 24. Xin, L.; Zhou, C.; Yang, Z.; Liu, D., Regulation of an Enzyme Cascade Reaction by a DNA Machine. *Small* **2013**, *9*, 3088-3091.
- 25. Agarwal, N. P.; Matthies, M.; Joffroy, B.; Schmidt, T. L., Structural Transformation of Wireframe DNA Origami *via* DNA Polymerase Assisted Gap-Filling. *ACS Nano* **2018**, *12*, 2546-2553.
- 26. Fu, J.; Liu, M.; Liu, Y.; Woodbury, N. W.; Yan, H., Interenzyme Substrate Diffusion for an Enzyme Cascade Organized on Spatially Addressable DNA Nanostructures. *J Am Chem Soc* **2012**, *134*, 5516-5519.
- 27. Zhao, Z.; Fu, J.; Dhakal, S.; Johnson-Buck, A.; Liu, M.; Zhang, T.; Woodbury, N. W.; Liu, Y.; Walter, N. G.; Yan, H., Nanocaged Enzymes with Enhanced Catalytic Activity and Increased Stability against Protease Digestion. *Nat Commun* **2016**, *7*, 10619.
- 28. Tian, Y.; Lhermitte, J. R.; Bai, L.; Vo, T.; Xin, H. L.; Li, H.; Li, R.; Fukuto, M.; Yager, K. G.; Kahn, J. S.; Xiong, Y.; Minevich, B.; Kumar, S. K.; Gang, O., Ordered Three-Dimensional Nanomaterials Using DNA-Prescribed and Valence-Controlled Material Voxels. *Nat Mater* **2020**, *19*, 789-796.
- 29. Klein, W. P.; Thomsen, R. P.; Turner, K. B.; Walper, S. A.; Vranish, J.; Kjems, J.; Ancona, M. G.; Medintz, I. L., Enhanced Catalysis from Multienzyme Cascades Assembled on a DNA Origami Triangle. *ACS Nano* **2019**, *13*, 13677-13689.
- 30. Ofer Idan, H. H., Origins of Activity Enhancement in Enzyme Cascades on Scaffolds. *ACS Nano* **2013**, *7*, 8658-8665.
- 31. Zhang, Y.; Hess, H., Toward Rational Design of High-efficiency Enzyme Cascades. *ACS Catal* **2017,** *7*, 6018-6027.
- 32. Zhang, Y.; Tsitkov, S.; Hess, H., Proximity does not Contribute to Activity Enhancement in the Glucose Oxidase-Horseradish Peroxidase Cascade. *Nat Commun* **2016,** *7*, 13982.
- 33. Gao, Y.; Roberts, C. C.; Toop, A.; Chang, C. E.; Wheeldon, I., Mechanisms of Enhanced Catalysis in Enzyme-DNA Nanostructures Revealed through Molecular Simulations and Experimental Analysis. *Chembiochem* **2016**, *17*, 1430-1436.
- 34. Gao, Y.; Roberts, C. C.; Zhu, J.; Lin, J.-L.; Chang, C.-e. A.; Wheeldon, I., Tuning Enzyme Kinetics through Designed Intermolecular Interactions Far from the Active Site. *ACS Catalysis* **2015**, *5*, 2149-2153.
- 35. Lin, J.-L.; Wheeldon, I., Kinetic Enhancements in DNA–Enzyme Nanostructures Mimic the Sabatier Principle. *ACS Catal* **2013**, *3*, 560-564.
- 36. Lang, X.; Hong, X.; Baker, C. A.; Otto, T. C.; Wheeldon, I., Molecular Binding Scaffolds Increase Local Substrate Concentration Enhancing the Enzymatic Hydrolysis of VX Nerve Agent. *Biotechnol Bioeng* **2020**, *117*, 1970-1978.
- 37. Breger, J. C.; Buckhout-White, S.; Walper, S. A.; Oh, E.; Susumu, K.; Ancona, M. G.; Medintz, I. L., Assembling High Activity Phosphotriesterase Composites Using Hybrid Nanoparticle Peptide-DNA Scaffolded Architectures. *Nano Futures* **2017**, *1*, 011002.
- 38. Tian, Y.; Wang, T.; Liu, W.; Xin, H. L.; Li, H.; Ke, Y.; Shih, W. M.; Gang, O., Prescribed Nanoparticle Cluster Architectures and Low-Dimensional Arrays Built Using Octahedral DNA Origami Frames. *Nat Nanotechnol* **2015**, *10*, 637-644.
- 39. Tian, Y.; Zhang, Y.; Wang, T.; Xin, H. L.; Li, H.; Gang, O., Lattice Engineering through Nanoparticle-DNA Frameworks. *Nat Mater* **2016**, *15*, 654-661.

- 40. Lin, Z.; Xiong, Y.; Xiang, S.; Gang, O., Controllable Covalent-Bound Nanoarchitectures from DNA Frames. *J Am Chem Soc* **2019**, *141*, 6797-6801.
- 41. Zafar, S.; Khater, M.; Jain, V.; Ning, T., A Comparison between Bipolar Transistor and Nanowire Field Effect Transistor Biosensors. *Appl. Phys. Lett* **2015**, *106*, 063701.
- 42. Zafar, S.; Lu, M.; Jagtiani, A., Comparison between Field Effect Transistors and Bipolar Junction Transistors as Transducers in Electrochemical Sensors. *Sci Rep* **2017**, *7*, 41430.
- 43. Das, P.; Zafar, S., Mechanistic Influence of Nanometer Length-Scale Surface Chemistry on DNA Hybridization. *ACS Nano* **2015**, *9*, 7466-7478.
- 44. Zafar, S.; Ning, T. In *Bipolar junction transistor based sensors for chemical and biological sensing*, 2016 46th European Solid-State Device Research Conference (ESSDERC), IEEE: 2016; p IEEE.
- 45. Kharitonov, A. B.; Zayats, M.; Lichtenstein, A.; Katz, E.; Willner, I., Enzyme Monolayer-Functionalized Field-Effect Transistors for Biosensor Applications. *Sens Actuators B Chem* **2000**, *70*, 222-231.
- 46. Douglas, S. M.; Dietz, H.; Liedl, T.; Hogberg, B.; Graf, F.; Shih, W. M., Self-Assembly of DNA into Nanoscale Three-Dimensional Shapes. *Nature* **2009**, *459*, 414-418.
- 47. Rothemund, P. W., Folding DNA to Create Nanoscale Shapes and Patterns. *Nature* **2006**, 440, 297-302.
- 48. Libertino, S.; Aiello, V.; Scandurra, A.; Renis, M.; Sinatra, F., Immobilization of the Enzyme Glucose Oxidase on Both Bulk and Porous SiO(2) Surfaces. *Sensors (Basel)* **2008**, *8*, 5637-5648.
- 49. Itoh, T.; Han, S.; Matsushita, Y.; Hayase, S., Enhanced Enantioselectivity and Remarkable Acceleration on the Lipase-Catalyzed Transesterification Using Novel Ionic Liquids. *Green Chemistry* **2004**, *6* (9), 437-439.
- 50. Wong, C. M.; Wong, K. H.; Chen, X. D., Glucose Oxidase: Natural Occurrence, Function, Properties and Industrial Applications. *Appl Microbiol Biotechnol* **2008**, *78*, 927-938.
- 51. Arslan, F.; Ustabas, S.; Arslan, H., An Amperometric Biosensor for Glucose Determination Prepared from Glucose Oxidase Immobilized in Polyaniline-Polyvinylsulfonate Film. *Sensors (Basel)* **2011**, *11*, 8152-8163.
- 52. Chi, C.; Vargas-Lara, F.; Tkachenko, A. V.; Starr, F. W.; Gang, O., Internal Structure of Nanoparticle Dimers Linked by DNA. *ACS Nano* **2012**, *6*, 6793-6802.
- 53. Abdallah, W.; Chirino, V.; Wheeldon, I.; Banta, S., Catalysis of Thermostable Alcohol Dehydrogenase Improved by Engineering the Microenvironment through Fusion with Supercharged Proteins. *Chembiochem* **2019**, *20*, 1827-1837.



For Table of Contents Only